Performance and failure analysis of full cell lithium ion battery with $LiNi_{0.8}Co_{0.15}Al_{0.05}O_2$ and silicon electrodes

Nils P. Wagner [a,b,*], Karina Asheim [a], Fride Vullum-Bruer [a], Ann Mari Svensson [a]

[a] Department of Material Science and Engineering Norwegian University of Science and Technology, NTNU, Norway
[b] Department of Sustainable Energy Technology, SINTEF Industry, Norway

HIGHLIGHTS

- Revealing degradation mechanisms in NCA.||Si Li-ion battery full cells.
- Full-cell Li-ion battery with Si anode showing up to 245 cycles at a high capacity.
- Lithium consumption is the main factor causing capacity fade in NCA.||Si full-cells.
- No material degradation of the full-cell cycled Si detected.

ARTICLE INFO

ABSTRACT

The influence of the lithium inventory on the performance and degradation mechanism of NCA||Si cells operating at a third of the theoretical silicon capacity is analysed. The lithium inventory was increased by electrochemical prelithiation to a value of 300 mAhg^{-1}(Si). Full-cells were cycled at harsh conditions with a cut-off of 4.4 V to maximise the capacity. The higher lithium inventory resulted in an increased reversible capacity from 163 to 199 mAhg^{-1}(NCA). The cycle-life was increased by 60% and reached 245 cycles. Three-electrode and post-mortem analyses revealed that the main reason for capacity fade is repeated SEI repair, consuming the lithium inventory. Differential capacity analysis revealed different degradation of silicon anodes cycled in half-cells compared to full-cells. No shifts in the alloying/dealloying peaks are present in full-cell geometry while changes are observed in half-cell geometry. This is expected to be caused by a limited alloying capacity in the full-cell and lithium consumption during cycling, alleviating material stresses. We conclude that the lithium consumption is the main factor causing capacity fade in NCA||Si cells. The decreasing degree of lithiation over cycling due to the lithium consumption is likely to be the reason for the absence of structural degradations of full-cell cycled silicon.

1. Introduction

Secondary lithium-ion batteries were commercialised in 1991 and are the dominating battery technology for portable devices and electric transportation. As they are the battery concept with the highest energy density on the market and most so-called post Li concepts are still in their infancy, optimisation of Li-ion batteries with respect to energy density, safety and price is a focus topic of the scientific community [1–4]. To increase the energy density on cell level, electrode materials with higher specific capacity are required. Currently, the main limiting factor is the moderate capacity available from the cathode materials, which can deliver between 120 and 200 mAhg^{-1}. Graphite, with a

specific capacity of 372 mAhg^{-1}, is the most common anode material in Li-ion batteries. In practical applications, the capacity value is lower, to mitigate the danger of Li plating towards the end of the lithiation. An anode material capable of delivering a capacity of about 1000 mAhg^{-1} is highly desirable, as it would increase the cell capacity by ~30% paired with a state of the art cathode delivering a capacity of 160 mAhg^{-1}. Another threefold increase in anode capacity would only raise the cell capacity by an additional 9%. Moreover, this is likely to be associated with other challenges. The increase in cell capacity by altering the anode does not directly translate to energy density, as this value is also dependent on the operating voltage of the electrodes and the density of the materials. The operating voltage should hence be close to that of

---

graphite, especially on anode delithiation. This rules out most conversion materials, since they show high voltage hystereses [5]. Silicon is believed to be a next generation anode material for Li-ion batteries, and it is already incorporated in low quantities (up to 12 wt%) in anodes of some commercial cells. Si is highly abundant and inexpensive and has a high theoretical capacity (3579 mAhg^{-1}), for the Li$_{15}$Si$_4$ alloy, which is formed below 50 mV. The average operating potential of a silicon anode is 0.4 V vs. Li/Li$^+$. The significant capacity advantages compared to graphite comes with the price of high volume expansion of over 300% upon Li uptake. This volume expansion hampers the implementation of silicon as anode as it causes the particles to crack or pulverise, as well as the loss of electrical wiring by detachment from the current collector. Upon extended cycling, severe changes in the silicon morphology and composition can be detected [6]. Lowering the particle size and/or limiting the Li uptake might remedy some of the issues by restraining the volume changes. Further means to reduce the degradation of silicon anodes are the use of high modulus biopolymer binders and or the encapsulation of silicon in different matrices [7–11].

In addition to morphological degradation, the volume changes cause cracking of the crucial SEI layer upon anode delithiation. This results in continuous SEI formation and repair consuming the electrolyte during cycling [12]. SEI forming additives such as fluoroethylene carbonate (FEC) and vinylene carbonate (VC) have significantly improved the cycling stability of silicon based electrodes by forming a more stable SEI [13,14]. FEC and VC decompose at higher potentials than the other electrolyte components and form a polymeric and LiF containing SEI on the anode surface [15–17]. FEC was also shown to have a positive effect on silicon based full-cells [18].

Some impressive improvements in cycle-life of silicon anodes was reported in the recent years, especially when limiting the lithiation [10, 19,20]. Yet, all these results were obtained in half-cell geometry vs. a highly over-dimensioned Li counter electrode, thereby masking irreversible consumption of Li ions, which is crucial in full-cell operation. Yim et al. calculated a maximum increase in gravimetric energy density of 59% when assuming only 6% irreversible loss. However, the authors stated immense difficulties in optimising Si graphite based full-cells, and their NMC||Si:graphite (10 wt% nano-Si) full-cell showed a capacity retention of only 63%, after 50 cycles [21]. The capacity fade mechanisms of LCO||Si alloy:graphite cells containing 15 wt% 3 M Si alloy were studied by Petibon et al. [22] The authors observed a slow capacity decay caused by the SEI repair and hence Li inventory loss, followed by a sudden failure at the point where the electrolyte was FEC depleted. Dupré et al. described the SEI evolution in NMC||Si cells and found non lithium containing organic species in the outermost regions of the SEI, pointing out that all available lithium was consumed [23]. Their full-cells contained a negative electrode consisting of 80% nano-Si and showed extreme capacity fading after only a few cycles. Two full-cell studies based on completely different electrode design by Beattie et al. and Ruther et al. concluded that parasitic side reactions consuming active lithium inventory was the main cause of the capacity fade [24, 25]. The authors of the former study analysed the potential evolution of NCA||Si full-cells with a high silicon content of 70 wt% μ-Si, whereas the latter study employed NMC/Si:graphite cells with 15 wt% nano-Si. The Li inventory loss of Si:graphite electrodes containing 15 wt% nano-Si was also studied by Dose et al. [26] Oversized LFP cathodes acted as artificial Li reservoir and allowed for the quantification of the Li loss. Accordingly, the amount of additional Li sources required to reach stable operation for 100 cycles was calculated and the need for SEI stabilisation was emphasised. Recently, Jin et al. reported an LCO||Si yolk-shell full-cell with self-healing SEI and a coulombic efficiency (CE) as high as 99.9%. The authors concluded that their design can essentially eliminate the Li inventory loss, yet their full-cell showed only 72% capacity retention after 100 cycles [27]. As silicon is a high capacity anode, it should be paired with high-energy cathodes to guarantee an increased overall specific energy.

Here, we demonstrate good cyclability of laboratory scale battery cells made from a low-cost, micron sized silicon material (60 wt% Si) and in-house made NCA cathodes. To highlight the importance of Li inventory, cells with pristine silicon were compared to cells with pre-conditioned and prelithiated anodes. Rather harsh cycling conditions were selected to enable the maximum capacity of the cathode.

In addition, the current study investigates the effect of the decreasing lithium inventory on the alloying mechanism, and the evolution of the individual electrode potential curves and end potentials upon cycling by three-electrode analysis. The evolution of the silicon potential curve in full-cell configuration is analysed by cycle resolved differential capacity analysis and directly compared to half-cell cycled silicon. Post-mortem cross sectional image analyses after 5, 50 and 100 cycles were performed to gain insight on changes of the silicon particles and the electrode structure upon cycling. Furthermore, electrochemical post-mortem XRD analysis performed on both electrodes after 5, 100 and 300 cycles in addition to post-mortem cycling in half-cells after 400 cycles in full-cell geometry. The combination of methods allowed for a better understanding of the capacity fade and degradation processes in the silicon anode.

2. Experimental

2.1. LiNi$_{0.8}$Co$_{0.15}$Al$_{0.05}$O$_2$ synthesis

LiNi$_{0.8}$Co$_{0.15}$Al$_{0.05}$O$_2$ (NCA) was synthesised by a sol-gel method applying citric acid as complexing agent. 40 mmol anhydrous LiNO$_3$(Alfa Aesar 99.98%), 32 mmol Ni(NO$_3$)$_2$ · 6H$_2$O (Sigma-Aldrich puriss. p.a., ≥98.5%), 6 mmol Co(NO$_3$)$_2$ · 6H$_2$O (Honeywell Fluka, ACS reagent, ≥99.0%) and 2 mmol Al(NO$_3$)$_3$ · 9H$_2$O (Sigma-Aldrich, ACS reagent, ≥98.0%) were dissolved in 100 mL deionised water under continuous stirring. 2 cation mol equivalent of citric acid were added and the solution was kept stirring at 120 °C until most of the solvent evaporated and a viscous gel formed. The gel was dried at 180 °C for 12 h and the resulting organic foam with embedded cations was thoroughly crushed with a pestle and mortar before it was calcined at 450 °C for 2 h to decompose the organic residues and the remaining nitrates. The calcined powder was ground again, and ultimately fired at 750 °C for 15 h under a constant flow of synthetic air.

2.2. Material characterisation

The synthesised NCA cathode material and the commercial Silgrain® e-Si 400 (ELKEM) material were structurally characterised by powder X-ray diffraction on a Bruker D8 Advance DAVINCI diffractometer working in Bragg−Brentano (Θ/2Θ) geometry with Cu Kα radiation. The XRD pattern of the synthesised layered oxide was refined using Topas (Bruker AXS Version 5). The particle size distribution of Silgrain® e-Si 400 was measured by laser diffraction on a Horiba LA-960. Additionally, the morphology of both materials and the b-site metal ratio of the synthesised NCA sample were studied by scanning electron microscopy and energy dispersive x-ray spectroscopy on a Hitachi SU-6600 equipped with a Bruker Quantax EDS.

2.3. Electrode and cell preparation and electrochemical and post-mortem characterisation

The NCA positive electrode blend consisted of 85 wt% synthesised NCA, 10 wt% conductive carbon black (Super C 65, Imerys) and 5 wt% PVDF (Kynar) as binder. The components were homogenised in N-methyl-2-pyrrolidone (NMP; Sigma-Aldrich, >99%). The silicon electrodes had a composition of 60 wt% silicon (Silgrain® e-Si 400, ELKEM), 10 wt% graphite (TIMREX® SLS 30, Imerys), 15 wt% conductive carbon black (TIMCAl C-NERGY™ Super C 65, Imerys) and 15 wt% carboxymethyl cellulose sodium salt (Na CMC, average Mw ~90,000, Aldrich). The Na CMC was dissolved in a citric acid/potassium citrate buffer at pH 3 to protonate the carboxyl groups of the CMC polymer and hence aid
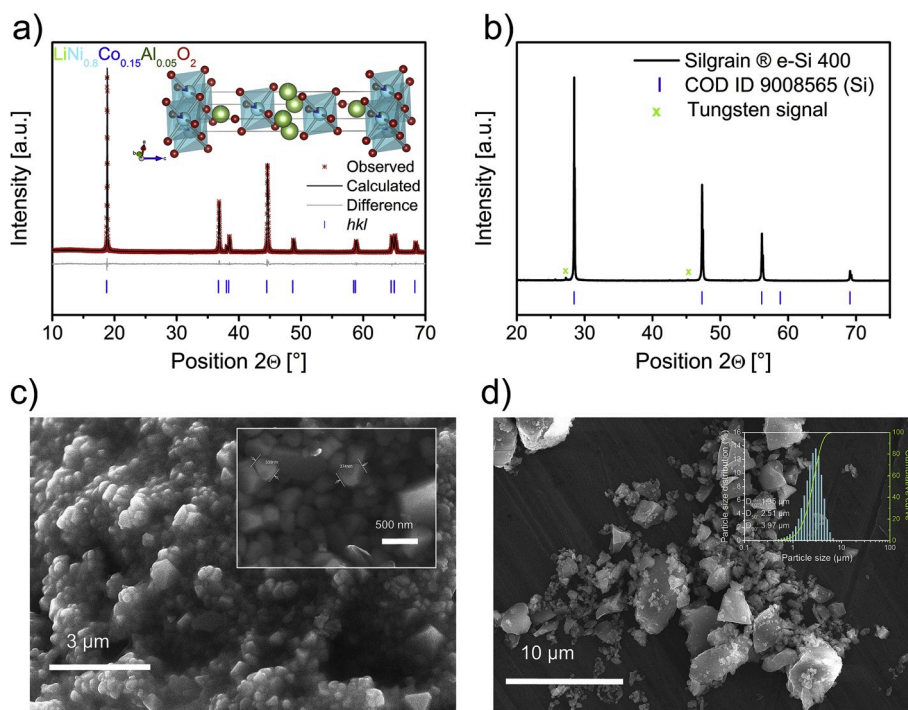
Fig. 1. Powder XRD results. a) Full pattern refinement of the NCA sample. b) Powder XRD pattern of Silgrain® e-Si 400 with underlying COD silicon reference. c) SEM micrograph of NCA with inset showing a higher magnification. d) SEM micrograph of Silgrain® e-Si 400 with particle size distribution in the inset.

the esterification reaction of the binder to the native oxide layer of the silicon particles [28–30]. The binder was dissolved in a ratio of 1:25 using a buffer stock solution containing 94.6 mmol L^{-1} citric acid (Sigma-Aldrich ACS reagent, ≥99.5%) and 37 mmol L^{-1} KOH (Sigma-Aldrich reagent grade, 90%) dissolved in deionised water. As the buffer chemicals remain in the cast after drying, the corrected mass ratio was 56:9:14:14:7 (Si:SLS30:Super C65:CMC:buffer). Positive NCA electrodes and negative Si electrodes were cast by slurry based tape casting on 25 μm thick Al foil (Alfa Aesar) and 20 μm thick dendritic Cu foil (Schlenk), respectively. The casted electrode sheets were pre-dried at 70 °C for 10 h in a drying cabinet. The final drying step was carried out under vacuum (90 °C for NCA, 110 °C for Si) for 10 h before circular electrodes (Ø = 16 mm) were cut and transferred to an Ar filled glove box ($O_2/H_2O < 0.1$ ppm). The anode to cathode (N/P) ratio was chosen in a manner that the Si negative electrode operates at about 1000–1200 mAhg^{-1}$_{(Si)}$ when the positive electrode delivers a capacity of 160 mAhg^{-1}$_{(NCA)}$. The average loading of the NCA electrodes was 3.5 mg$_{(NCA)}$ cm^{-2}, and the corresponding silicon electrodes had an average loading of 0.6 mg$_{(Si)}$ cm^{-2}. Half- and full-cell testing was carried out in CR 2016 coin cells using a porous polypropylene separator (Celgard 2400) and 40 μl electrolyte consisting of 1 M LiPF$_6$ in EC/PC/DEC (1:1:3 by weight). As SEI forming additives, 1 wt% VC and 5 wt% FEC were added to the electrolyte. (LiPF$_6$ and carbonate solvents and additives were from Sigma Aldrich in battery grade. Galvanostatic experiments were carried out on a LANHE CT 2001A and a Maccor model 4200 at 20 °C. 160 mA g^{-1} was defined as 1 C for NCA and 3600 mA g^{-1} for silicon. As different potential windows were used, the applied potential windows are given in the corresponding results and discussion chapter. Full-cells investigated post-mortem by half-cell electrochemical cycling, were opened after 400 cycles in an Ar filled glove box. The electrodes were carefully detached and both the NCA and silicon electrodes were re-assembled in half-cell configuration using the same parameters as described above. In order not to damage or remove any SEI, the electrodes were not rinsed. The same procedure was employed for ex situ cross sectional FIB-SEM analysis of silicon electrodes after different cycle numbers. Cross sectional analysis was done on a FEI Helios

NanoLab DualBeam FIB. In addition, post-mortem XRD patterns, of both cathode and anode, were recorded after different cycle numbers using the same setup as described above. The electrodes were fixed on silicon single crystal sample holders and the patterns were refined using the structureless Pawley method to correct the height error and calculate unit cell parameters of the NCA cathode. Three-electrode analysis was performed in PAT-Cells (EL-CELL Germany) with a Li reference using a glass fibre separator and 100 μL of the above-mentioned electrolyte. Three electrode cycling was performed on a VMP 300 potentiostat (Bio-Logic).

3. Results and discussion

A full pattern refinement of the synthesised NCA, the powder x-ray diffractogram and SEM micrographs of the synthesised NCA and the commercial silicon are shown in Fig. 1. The silicon particle size distribution is shown in the inset of Fig. 1 d). The powder x-ray pattern of the synthesised NCA was fitted to the layered α-NaFeO$_2$ in the rhombohedral space group R-3m. The lattice parameters were refined to a = b = 2.8651 Å and c = 14.1848 Å and the Li/Ni site exchange is as low as 1%. The commercial silicon powder is phase pure crystalline silicon as shown in Fig. 1 b). The additional peaks correspond to tungsten, which is a contamination signal from the X-ray tube.

The NCA powders consist of agglomerated primary particles in the range of 300–400 nm. The particle morphology ranged between spherical to octahedral with visible crystal facets. The b-site metal ratio was measured by EDS. The average of five measurements gave a ratio of 82 at.% Ni, 14 at.% Co and 4 at.% Al. This corresponds well to the nominal stoichiometry of LiNi$_{0.8}$Co$_{0.15}$Al$_{0.05}$O$_2$. The d50 value of the silicon was calculated to be 2.51 μm and the particle size distribution was monodisperse ranging from 450 nm to 7 μm with the majority of particles in the μm regime. SEM micrographs, as shown in Fig. 1 d), further confirmed this.

Prior to full-cell analysis, the performance of NCA and silicon was examined in half-cell setup vs. metallic Li. Fig. 2 summarises the cycling data of both half-cells. The voltage profile, rate performance and long-
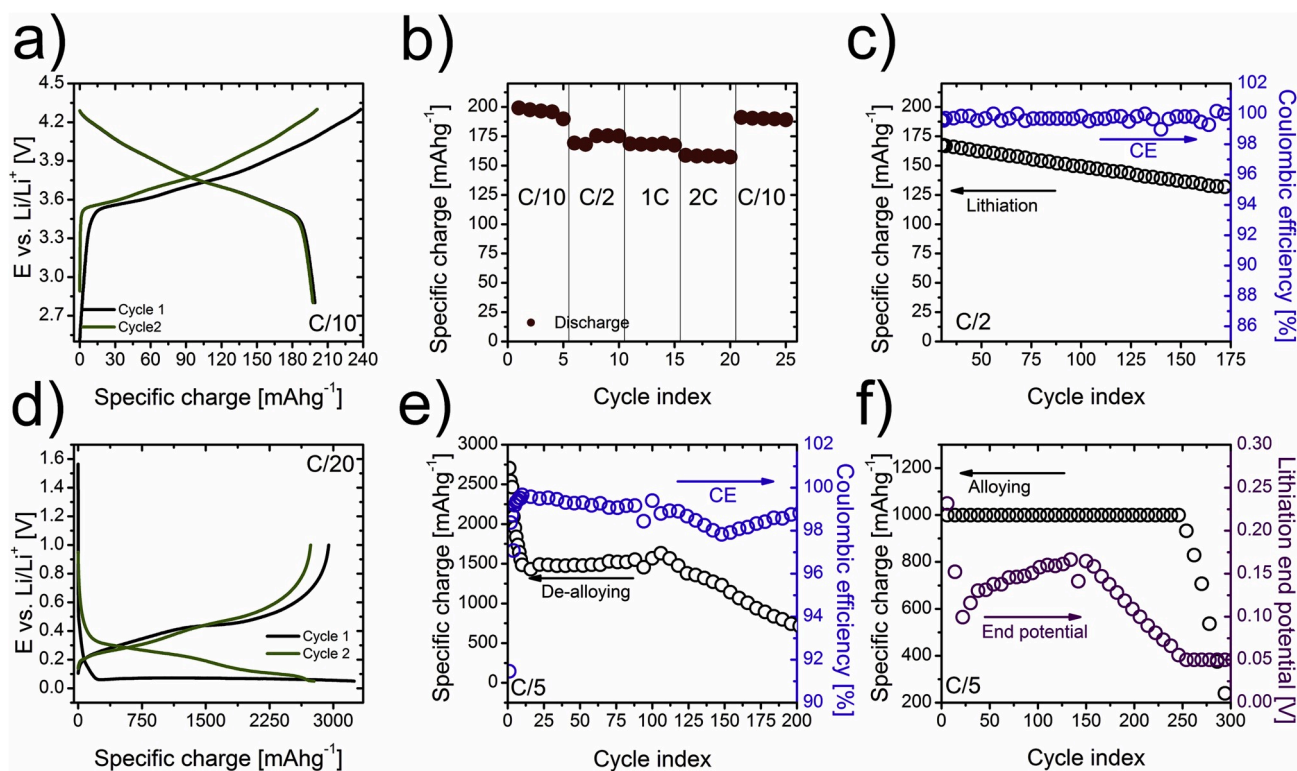
Fig. 2. Cycling data in half-cell configuration. a) Voltage profile of the first two cycles of a NCA half-cell recorded at C/10. b) Rate performance of the NCA half-cell. Note maximum charge rate was set to C/2. c) Long term cycling of an NCA half-cell at C/2 with coulombic efficiency (CE). d) Voltage profile of the first two cycles of a silicon half-cell recorded at C/20. e) Long term cycling of a silicon half-cell at C/5 with CE. f) Lithiation limited cycling of a silicon half-cell at C/5 including the potential at which the lithiation reached an equivalent of 1000 mAhg^{-1}$_{(Si)}$.

time cycling of NCA are shown in a-c). Cycled between 2.8 and 4.3 V at a low rate of C/10 the NCA electrode delivered a first cycle discharge capacity of 199 mAhg^{-1} and a first cycle efficiency of 84%. The relatively low first cycle efficiency might be caused by some side reactions upon the first charge between OCV and 3.3 V and by the formation of a cathode interface. In the second cycle the coulombic efficiency (CE) increased to 98%. Fig. 2 b) shows the discharge capacity of the NCA electrode at different rates. The investigated discharge rates were C/10, C/2, 1C and 2C for 5 cycles each. After cycling at 2C the discharge rate was lowered to C/10 again to analyse the capacity recovery. The maximum rate on charge was set to C/2 in constant current mode. The NCA electrode showed good rate performance and delivered a high capacity of 160 mAhg^{-1} even at a high discharge rate of 2C. After switching to a low rate of C/10 after 20 cycles, the NCA electrode recovered 97% of its initial capacity. Fig. 2 c) shows the long-term cycle behaviour at C/2, which was performed after the rate test. The capacity retention after 175 cycles was 79% with an average CE of 99.7%.

Cycling data of the silicon half-cell are shown in Fig. 2 d-f). Fig. 2d) shows the first two formation cycles at a low rate of C/20 in a potential window of 0.05–1 V. The distinct difference between the first and second lithiation (discharge) voltage profiles is due to the conversion of crystalline to amorphous silicon during the first lithiation. The capacity achieved during the first lithiation was 3245 mAhg^{-1}$_{(Si)}$ and the irreversible charge loss was as low as 9.2%. After two formation cycles, the rate was increased to C/5 (0.72 Ag^{-1}) and the silicon half-cell was cycled in the aforementioned potential window. A cut-off potential of 0.05 V was chosen to hinder crystallisation of a Li$_{15}$Si$_4$ phase. Upon cycling at C/5 the capacity dropped during the first 12 cycles to a value of about 1500 mAhg^{-1}$_{(Si)}$, where it stabilised. At the same time, the CE approached values of >99.5%. The silicon half-cell exhibited stable cycling behaviour at a capacity of 1500 mAhg^{-1} for 100 cycles with an average CE of 99.3%. Afterwards, a steep drop in capacity, accommodated by a drop in the CE was observed. This phenomenon was

previously described as the point of FEC depletion of the electrolyte [31]. Fig. 2 f) shows the performance of a silicon half-cell at C/5, where the lithiation was limited to 1000 mAhg^{-1}$_{(Si)}$. The ultimate lower cut-off potential was set to 0.05 V and the evolution of the lithiation end potential equivalent to 1000 mAhg^{-1}$_{(Si)}$ was monitored during cycling. Under these conditions, the silicon half-cell delivered the set capacity for 249 cycles. The lithiation end potential initially showed a steep drop from 0.23 V to 0.1 V during the first 15 cycles. During the following 140 cycles a slow increase in the lithiation end potential of 50 mV was detected before it declined again to meet the ultimate cut-off after 249 cycles. At cycle 155, a simultaneous decline in the lithiation end potential and a drop in the CE from >99 to 98% was observed (Fig. S1 supplementary information). A drop in the end potential indicates degradation of the electrode, causing a higher overpotential. In addition, the point where the end potential drops might well be correlated with the consumption of the SEI forming additives FEC and VC. This will lead to the reduction of the other electrolyte solvents and hence an even thicker SEI. The voltage profiles of cycle 5, 50, 100, 150 and 200 are shown in the supplementary information (Fig. S2). The shifts in both the lithiation and delithiation profiles between cycle 150 and 200 suggest not only increased overpotentials but also a shift from the reaction a-Si → Li$_{2+x}$Si towards a-Li$_{2+x}$Si→ a-Li$_{3.5+x}$Si [32–35].

In a half-cell configuration, the huge Li excess of the Li counter electrode will mask Li loss in the anode and/or the SEI. In order to verify if the performance and degradation behaviour are translatable to full Li-ion cells, NCA||Si cells were assembled. The electrodes were balanced such that a charge of 160 mAhg^{-1}$_{(NCA)}$ equals a charge of 1000–1200 mAhg^{-1}$_{(Si)}$. As our aim was to evaluate the performance and failure of cells with a high specific energy, a rather wide voltage window (2.2–4.4 V) was chosen. The formation of an SEI layer on both electrodes upon the first charge will consume some of the available Li ions and hence cause a first cycle inefficiency and a reduced discharge capacity. To counter act the interphase formation on the anode side, cells with a
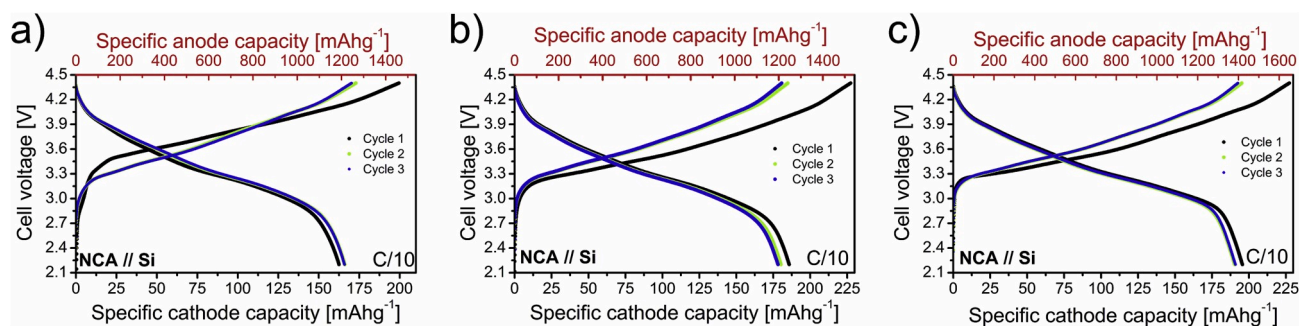
Fig. 3. Voltage profiles of the first three cycles of NCA‖Si full-cells recorded at C/10. a) Pristine NCA‖Si full-cell. b) Preconditioned NCA‖Si full-cell. c) Prelithiated NCA‖Si full-cell.
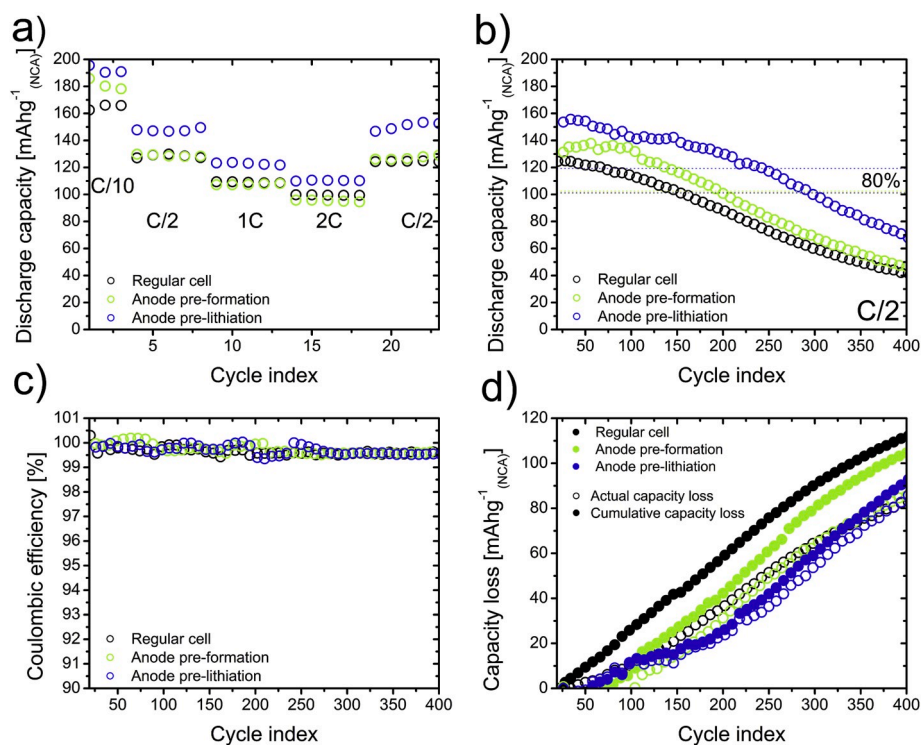

Fig. 4. Rate performance and long term cycling results of NCA‖Si cells. a) Rate performance of NCA‖Si cells from C/10 to 2C in cc mode where the maximal C-rate on charge is 1C. b) 400 cycles at C/2 of NCA‖Si cells. The dotted lines indicate 80% of the initial capacity at C/2. c) Corresponding coulombic efficiencies. d) Comparison of the cumulative and the actual capacity loss over 400 cycles.

silicon anode that underwent a formation cycle in a half-cell (termed preconditioned full-cell) and cells that underwent a formation cycle and a prelithiation to a level of 300 mAhg^{-1}$_{(Si)}$ (termed prelithiated full-cell) were investigated in addition to cells with pristine anode and cathode (termed pristine full-cell). Fig. 3 a-c) shows the voltage profiles of the first three cycles of pristine, preconditioned and prelithiated NCA‖Si full-cells.

The full-cell voltage profile is shifted to lower voltages compared to graphite based cells, as the de/lithiation potential of silicon is located roughly 0.3–0.4 V higher than the graphite intercalation potential. Hence, the lower cut-off was adjusted to allow for full relithiation of the cathode. The first cycle discharge capacity of the pristine, the preconditioned and the prelithiated full-cells were 163, 189 and 199 mAhg^{-1}$_{(NCA)}$ with a first cycle efficiency of 81, 82 and 86%, respectively. The first cycle efficiency of the former two full-cells is lower than the efficiency of the NCA half-cell. This corresponds to the formation of interphases on both electrodes and some oxidative decomposition of the electrolyte. In the latter two cells, the initial formation of the SEI was done in a half-cell prior to full-cell assembly. Thus, the first cycle inefficiency is caused by the formation of a cathode interphase, electrolyte oxidation and likely the formation and repair of the SEI due to the volume expansion/contraction of silicon. In the case of the prelithiated full-cell, the additional lithium can counteract the irreversible lithium loss upon the first charge. The pristine full-cell showed a distinct different voltage profile upon the first charge. The sloping profile between 2.8 and 3.3 V is caused by the SEI formation on the anode, while the general difference in slope and the higher location of the first charging potential is caused by the lithiation of crystalline silicon and the consequent amorphization upon the first charge. The first cycle discharge capacities translate to a silicon delithiation capacity of 1189, 1248 and 1419 mAhg^{-1}$_{(Si)}$, respectively. The prelithiated full-cell achieved the highest specific energy of 583 mWhg^{-1} $_{(active\ materials)}$. This corresponds to 461 mWhg^{-1} of electrode masses. The other specific energies are given in the supplementary information (Table S1).

Fig. 4 a-d) summarises the rate performance and cycle life of the three different NCA‖Si cells. The cell with the anode that underwent a
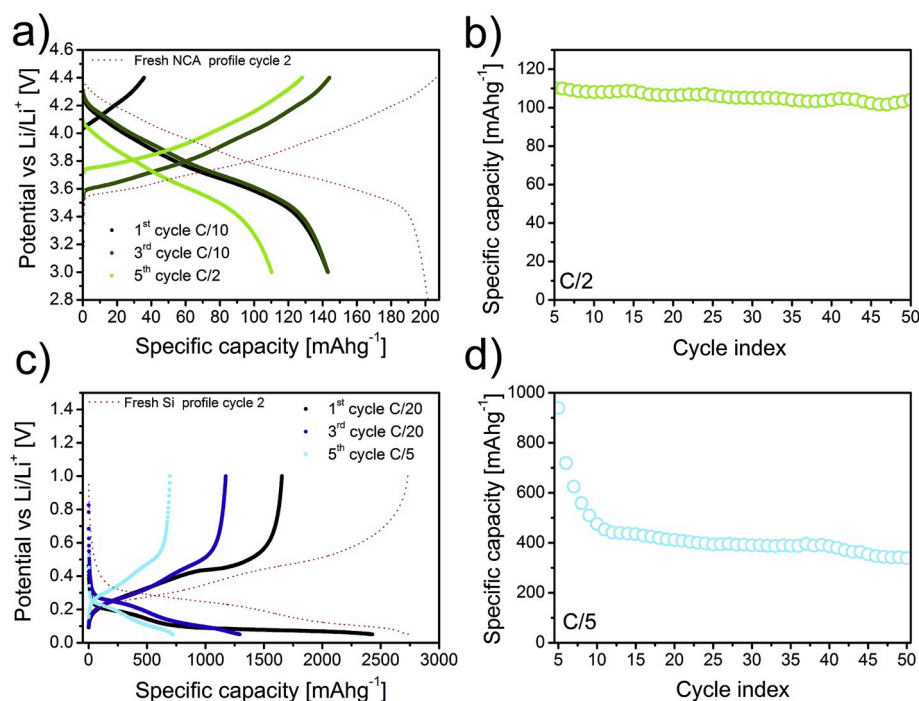
Fig. 5. Post-mortem cycling of NCA and silicon in half-cell configuration vs. a Li electrode a) 1st, 3rd and 6th cycle voltage profiles of NCA including the second cycle voltage profile of a fresh half-cell as guide for the eye. b) 50 cycles at C/2 of NCA, c) 1st, 3rd and 6th cycles voltage profile of silicon including the second cycle voltage profile of a fresh half-cell as guide for the eye. d) 50 cycles at C/5 of silicon.

preconditioning showed a similar rate performance as the pristine full-cell, despite of the higher initial capacity at C/10. The cells delivered reversible discharge capacities of about 130, 110 and 100 mAhg^{-1}$_{(NCA)}$ at C/2, 1C and 2C, respectively. The prelithiation improved the capacity and the cell delivered reversible discharge capacities of 150, 125 and 110 mAhg^{-1}$_{(NCA)}$ at the aforementioned rates. The rate performance is in fact very similar, but the prelithiated full-cell delivers a higher capacity due to the presence of sufficient amounts of Li for full relithiation of the cathode. After the assessment of the rate performance, the cells underwent a long-term cycling (study) for 400 cycles at C/2. The discharge capacities and the corresponding CEs are given in Fig. 4b) and c), respectively. Fig. 4 b) includes a dotted line indicating the point where the capacity has dropped to 80% of the initial value at C/2. This was the case after 153, 196 or 245 cycles for the full-cell with pristine, preconditioned and prelithiated anode, respectively. The coulombic efficiency ranged between 99 and 100% in all cases. The pristine full-cell showed stable cycling at a discharge capacity of 125 mAhg^{-1}$_{(NCA)}$ for 35 cycles before the capacity started to fade slowly. The preconditioned full-cell exhibited stable cycling behaviour for 100 cycles at 135 mAhg^{-1}$_{(NCA)}$, before the capacity faded in the same manner. After 400 cycles, both cells showed a remaining capacity of 40 and 45 mAhg^{-1}$_{(NCA)}$, respectively.

The improved lifetime might be explained by the fact that the preconditioned full-cell contained a higher degree of additives in the electrolyte, as the initial SEI formation was done in a half-cell. The prelithiated full-cell showed an even higher discharge capacity of 155 mAhg^{-1}$_{(NCA)}$ for 50 cycles before the onset of capacity decay was observed. The decay was less than for the other two cells, and the cell exhibited significantly improved lifetime. As the anode was prelithiated electrochemically, both the active Li inventory and the amount of electrolyte additives are higher compared to the pristine full-cell. The capacity of this cell is higher, as no Li is lost in the initial formation of the SEI and the loss of Li in the cathode interphase formation can be compensated by Li ions from the anode. The higher operating capacity on the other hand, and the fact that the anode is partially lithiated might be responsible for the earlier onset of capacity decay in comparison to

the preconditioned full-cell. Even though the onset was earlier, the capacity decay was less pronounced, which again can be caused by partial compensation of Li from the anode. After 400 cycles, the remaining capacity was 70 mAhg^{-1}$_{(NCA)}$. In half-cell studies it has often been reported that smaller silicon particles show increased cyclability as they can withstand the volume changes upon alloying with Li. Liu et al. defined a critical particle size of 150 nm, below which the lithiation of silicon does not lead to particle cracking [36]. However, nanoparticles have a high surface area, which results in increased SEI formation and hence Li loss. A recent study analysed sub-micron sized silicon recovered from diamond wire wafer cutting in half- and full-cell geometry [37]. Here, the half-cell showed adequate cyclability, while the capacity of the NMC∥Si full cells decayed rapidly. The lower surface area of the silicon anode and hence the lower amount of SEI formation and repair in the current study is likely to cause the increased cyclability of our NCA∥Si cells. Fig. 4 d) compares the apparent and the cumulative capacity loss of all three cells and it is visible that all cells lost about 85 mAhg^{-1}$_{(NCA)}$. The cumulative loss is the sum of the coulombic inefficiency over all cycles and is in all cases higher than the actual loss. In case of the pristine full-cell and the preconditioned full-cell it is significantly higher. Since silicon has a sloping voltage profile, lower degrees of lithiation will shift also the cathode cut-off to higher potentials vs. Li/Li$^+$. Any parasitic side reaction that does not degrade the active materials or consume accessible Li will be visible in the cumulative loss. Those side reactions can for example be the oxidation of solvent molecules at high potential. As the prelithiated anode does not operate from a SOC = 0, but SOC = 8.3% (300 mAhg^{-1}$_{(Si)}$), the end of lithiation happens at a higher SOC, and hence the cathode cut-off will occur at lower potentials vs. Li/Li$^+$. This will cause a lower degree of electrolyte oxidation and thus a lower cumulative loss compared to the pristine and preconditioned full-cell.

Fig. 5 a-d) shows the voltage profile and the capacity retention for 50 cycles of an NCA cathode and a silicon anode which have been reconfigured in a half-cell setup after 400 cycles of full-cell operation. The second cycle voltage profile of fresh NCA and silicon half-cells was added as guide for the eye. It clearly reveals that the irreversible consumption of Li ions is the main reason for the capacity fade in the full-
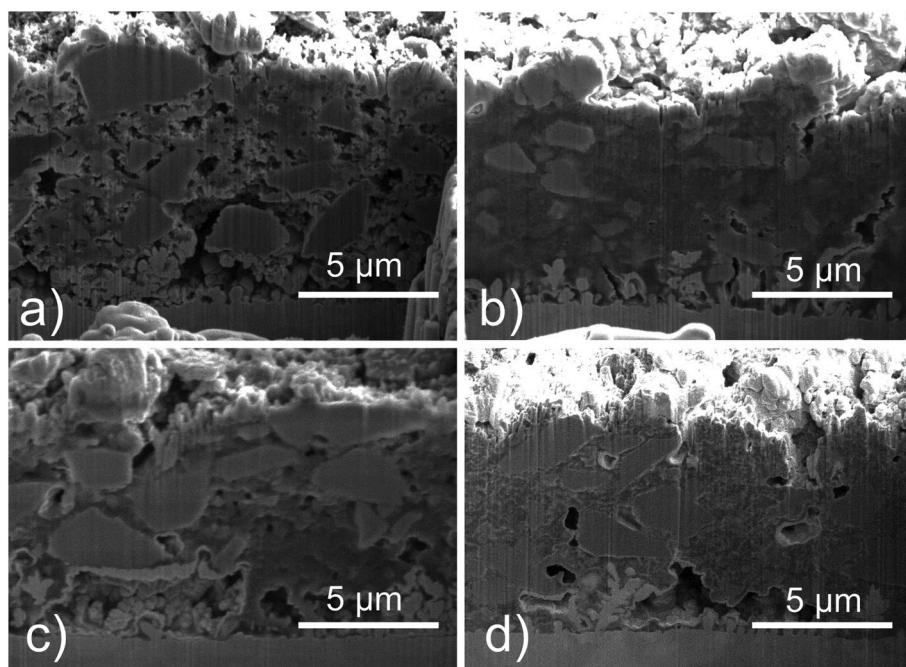
Fig. 6. Focused ion beam cross sectional SEM analysis of silicon anodes. a) pristine, b) after 5 cycles in full-cell configuration, c) after 50 cycles in full-cell configuration, d) after 100 cycles in full-cell configuration.

cell. The NCA voltage profiles for the 1st, 3rd and 6th cycle at C/10 and C/2, respectively, are shown in Fig. 5 a). The cell exhibited an OCV = 4.03 V, indicating a high SOC of the cathode. When charged to

4.4 V, the delithiation capacity was 36 mAhg^{-1}$_{(NCA)}$. This value corresponds well to the remaining capacity of the full-cells after 400 cycles (~40 mAhg^{-1}$_{(NCA)}$). The slightly lower capacity value of NCA in the
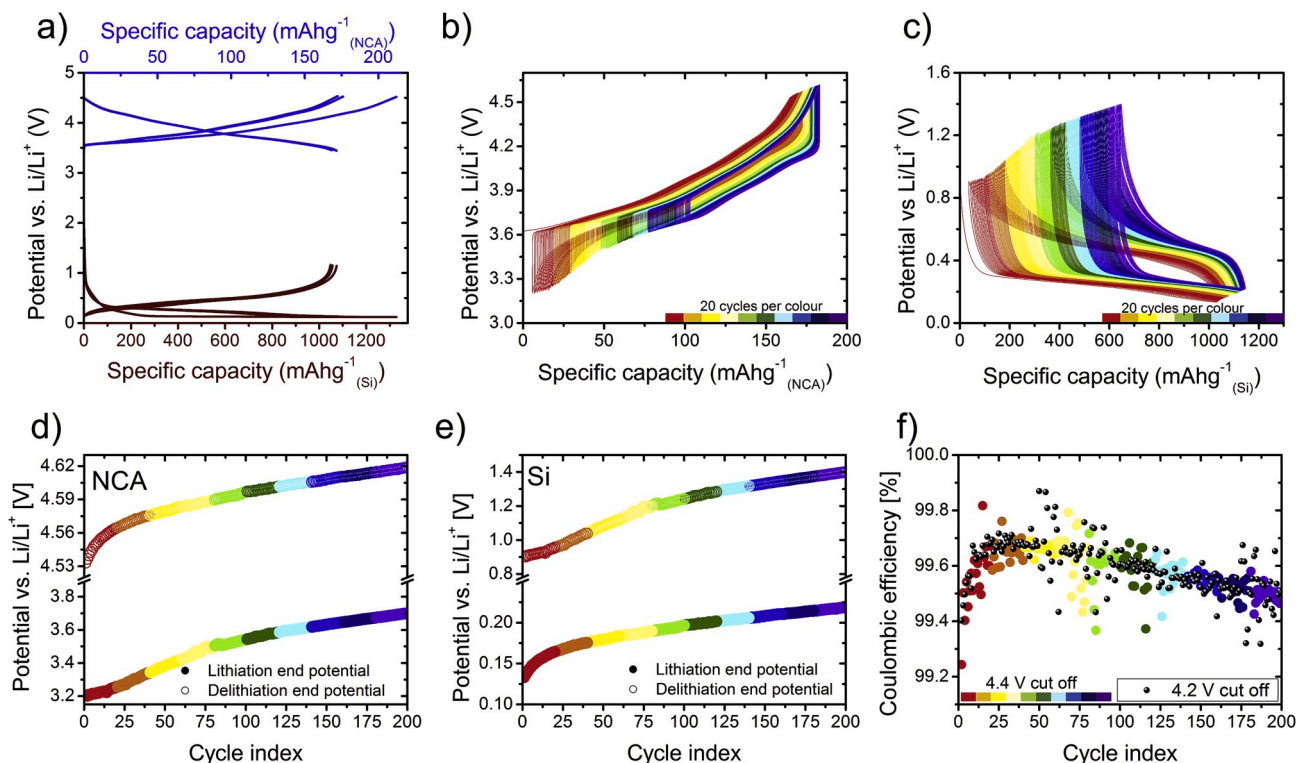

Fig. 7. Three electrode cycling of an NCA||Si cell with a Li reference between 2.3 and 4.4 V. a) Voltage profile of NCA and silicon vs. Li/Li$^+$ upon the first three formation cycles at C/10. b) NCA voltage profile for 200 cycles where each colour represents 20 cycles. c) Silicon voltage profile for 200 cycles where each colour represents 20 cycles. d) Evolution of the upper and lower cut-off potential of the NCA electrode vs. Li/Li$^+$ with the same colour code. e) Evolution of the upper and lower cut-off potentials of the silicon electrode vs. Li/Li$^+$ with the same colour code. f) Coulombic efficiency over 200 cycles with the same colour code. The black symbols show a cell that was cycled to 4.2 V. (For interpretation of the references to colour in this figure legend, the reader is referred to the Web version of this article.)

half-cell can be explained by the fact that the upper cut-off of 4.4 V will be slightly lower when measured vs Li/Li^+ compared to silicon. As the NCA cathode was polarised to high potentials for 400 cycles, some degradation is expected. Nevertheless, the NCA cathode still delivered a reversible discharge capacity of 143 mAhg^{-1}$_{(NCA)}$ at C/10. The average discharge potential was 3.71 V, which is only 0.04 V lower than the average potential of the fresh electrode. At C/2 the capacity was 110 mAhg^{-1}$_{(NCA)}$, and stable for 50 cycles (Fig. 5 b).

The capacity upon first lithiation of the reassembled silicon anode in half-cell configuration reached a high value of 2430 mAhg^{-1}$_{(Si)}$ at C/20 (Fig. 5 c). However, only 1660 mAhg^{-1}$_{(Si)}$ were reversible upon delithiation. Furthermore, the lithiation voltage profile shifts towards lower voltages compared to a fresh cell. This could be caused by an increased overpotential of the cycled silicon due to the thick SEI layer, or by a shift in the reaction as previously described. When increasing the current, the capacity quickly dropped to values of 400 mAhg^{-1}$_{(Si)}$ (Fig. 5d).

The difference in lithiation capacity of a fresh half-cell and the half-cell after 400 full-cell cycles can be explained by a number of reasons. Some parts of the electrode might be electronically insulated by the SEI, and parts of the silicon can be inactive by the formation of SiO_xF_y and Li_4SiO_4 phases on the silicon surface [38]. However, the high degree of lithiation in a half-cell after 400 full-cell cycles suggests that the amount of Li trapped in the silicon particles is rather limited, and a majority of the Li will be trapped in the SEI matrix. Fig. 6 shows cross sectional FIB-SEM micrographs of silicon anodes after 0 (a), 5 (b), 50 (c) and 100 (d) cycles in full-cell operation. The fresh anode consists of a porous network of silicon particles in a network of carbon black, graphite and Na CMC binder. Already after 5 cycles, this network is highly densified by the SEI.

Upon further cycling, the network is further densified, and after 100 cycles there is virtually no open porosity left in the electrode, and further SEI is likely to form on the outer surface of the electrode. There was not much of an increase in electrode thickness observed, nor any severe change in the silicon morphology as was reported in half-cell tests [6, 39]. This is probably due to the limited lithiation to about 1000 mAhg^{-1}$_{(Si)}$ and the steadily decreasing capacity causing volume change related stresses to alleviate upon cycling. Pawley fitted XRD patterns of cycled silicon anodes and NCA cathodes and the evolution of the NCA lattice parameters 0, 5, 100 and 300 cycles are shown in the supplementary information. (Fig. S3 and Table S2). The Li content in the NCA cathode is decreasing with increasing cycle number as discussed above. This can be directly monitored by the decrease in lattice parameter A and increased in lattice parameter C [40]. The N/P ratio of the electrodes in this study were chosen in a manner that graphite should not partake in the electrochemical reaction. Hence, the ratio of the graphite *002* to the silicon *111* peak was used to monitor the silicon amorphization over cycling. The pristine anode had a peak ratio of 0.4. After 5 cycles the ratio decreased to 0.3 and stayed at this value. This data suggests that the silicon particles are not completely lithiated but keep a crystalline core that does not partake in the lithiation reaction. The degree of lithiation is decreasing over cycling as Li is trapped in the SEI. As a result of this, no further amorphization of the silicon particles is observed. To monitor the loss of Li and to examine how it affects the voltage profiles and the cut-off potentials of both electrodes, an NCA‖Si three electrode PAT-Cell (EL-Cell Germany) was cycled in a potential range of 2.3–4.4 V while both anode and cathode potentials were monitored vs. Li/Li^+. The results are summarised in Fig. 7, where a) shows the voltage profile of NCA and silicon upon the first three formation cycles at C/10, b) and c) show the evolution of the voltage profile of NCA and silicon over 200 cycles, while d) and e) show the corresponding cut-off potential evolution vs. Li/Li^+. The corresponding full-cell profiles are shown in the supplementary information (Fig. S4). The evolution of the CE is shown in Fig. 7 f) and compared to a cell that was cycled to 4.2 V.

The anode lithiation end potential never dropped below 0 V vs. Li/Li^+, we can hence exclude Li plating upon cell operation. The first cycle

efficiency of the three-electrode cell was 81%, where the reversible cathode capacity was 170 mAhg^{-1}$_{(NCA)}$ with the corresponding anode capacity of 1070 mAhg^{-1}$_{(Si)}$. While the end potential of the anode after the first cycle was 1.13 V vs. Li/Li^+ with a distinct polarisation feature at the end of delithiation, the cathode end potential was 3.44 V vs. Li/Li^+ and did not show strong concentration polarisation. The three-electrode setup allows to directly monitor the lack of full relithiation of the cathode due to Li loss in the SEI. Upon switching to a cycling rate of C/2, the polarisation and hence the end potentials shift slightly. It is noteworthy that the rate performance in the PAT-Cell setup was enhanced, most likely due to increased pressure in this setup. Fig. 7b) and c) show that the overall drift over 200 cycles was only 18.4 mAhg^{-1}$_{(NCA)}$, which is equivalent to 115 mAhg^{-1}$_{(Si)}$. However, the loss of active Li becomes apparent from the evolution of the voltage profiles. The SOC of the NCA is steadily increasing during cycling. Furthermore, the polarisation of the NCA cathode increases from 50 mV over the course of 200 cycles. This is likely linked to the exposure to high potentials causing some degradation of the cathode. At the same time, the voltage profile of silicon shows increased concentration polarisation at the end of delithiation. As the discharge cut-off was set to 2.3 V, the electrode is polarised to reach this value, as the NCA cathode cannot be fully relithiated. Hence, the changes in end potentials of both electrodes are directly linked (Fig. 7 d-e). At the end of discharge, the potential of the NCA cathode is initially at 3.2 V vs. Li/Li^+. The Li loss causes the SOC to increase in the fully discharged state upon cycling. After 200 cycles, the potential of the NCA at the end of discharge is shifted to 3.7 V vs. Li/Li^+. Accordingly, to reach the cell cut-off, the silicon anode has to polarise to 1.4 V vs. Li/Li^+ since it cannot deliver any more Li ions. Contrary to graphite, the alloying of silicon is characterised by a sloping voltage profile. As Li is lost in the SEI over cycling, the degree of lithiation is decreasing and hence the end potential shifts to higher values. This will shift the delithiation potential of NCA to higher values. The initial upper potential of the NCA cathode was 4.53 V vs. Li/Li^+. After 200 cycles, this potential was shifted to 4.62 V vs. Li/Li^+. This high potential will promote electrolyte oxidation and surface instabilities of the NCA cathode, at the same time the ever-increasing upper cut-off potential will cause further delithiation of NCA, keeping the CE artificially high. Beattie et al. previously discussed this phenomenon [24]. In their study, the authors applied different cut-off voltages (3–4.2 V) and described a strong dependency of the CE on the upper cut-off. When the authors increased the upper cut-off to 4.3 V, they observed a highly reduced CE. We did not observe this trend, likely because no constant voltage step at high potentials was applied in this study. Fig. 7 f) shows the evolution of the CE over cycle life for a cell cycled to 4.2 and to 4.4 V. Both CE profiles look identical. Over the course of the first 25 cycles the CE increases from 99.2 to 99.7%, probably caused by the liberation of new Li ions from the NCA cathode as the cut-off potential increases. Afterwards the CE slowly decreases to a value of 99.5% over the 200 cycles, caused by side reactions at high potentials and continuous Li loss in the anode SEI. The relatively high CE even at these high potentials is achieved by the liberation of Li ions due to the rising potential and probably by a protective cathode interface caused by the initial oxidative degradation of electrolyte species. The liberation of additional Li ions is only possible in layered oxides that will be only partly delithiated upon cycling. Thus, the pairing of silicon anodes with cathodes that can be completely delithiated such as LMO or LFP will decrease the cycle-life, because the Li inventory loss cannot be counterbalanced by further delithiation of the cathode [26].

It is proven that the main reason for capacity fade of silicon based anodes in full-cell configuration is the irreversible loss of active Li species in the SEI. This is directly linked to the volume changes upon (de)lithiation causing the SEI instability. In half-cell studies this phenomenon is masked by the Li counter electrode but is apparent by a low CE. We furthermore compared the evolution of the silicon voltage profile in half and full-cell configuration. To increase the readability and conclusiveness we chose the dQ/dV contour representation for 200 cycles with
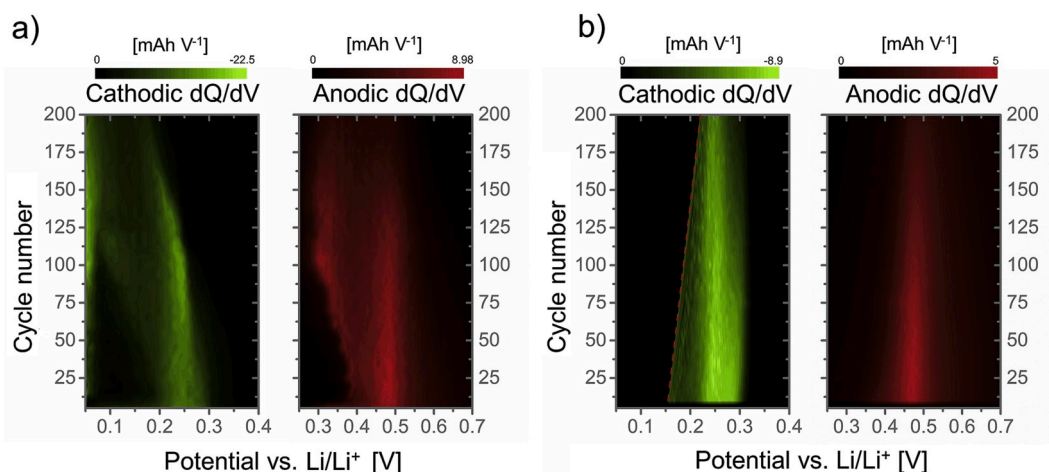
Fig. 8. Contour representation of the dQ/dV profile evolution over 200 cycles of silicon in half-cell (a) and in full-cell configuration (b). The green contour plot shows the cathodic signal (lithiation of silicon) and the red contour shows the anodic signal (delithiation of silicon). The red dotted line in b) indicates the end of lithiation potential. The area beyond this point was coloured to ease the readability. (For interpretation of the references to colour in this figure legend, the reader is referred to the Web version of this article.)

a resolution of 5 cycles. Fig. 8a) and b) show the evolution of the cathodic and anodic dQ/dV profile of the corresponding silicon electrodes. In both setups the capacity during early cycles can be attributed to the reaction a-Si ↔ a Li$_{2+x}$Si, which occurs at 0.25 V upon lithiation and at 0.47 V upon delithiation [33]. In the half-cell, we observe a clear shift over cycling towards the reaction Li$_{2+x}$Si ↔ Li$_{3.5+x}$Si. This becomes very visible in the dQ/dV plot at about 100 cycles.

At the same time, the capacity begins to fade. This point probably reflects the depletion of additives in the electrolyte. As previously mentioned, a recent study by Wetjen et al. showed the severe changes in silicon morphology upon cycling with an oversized LFP cathode [6]. The changes in morphology and increased surface area allow for deeper lithiation and after cycle 100 the dQ/dV clearly shows the footprint of the Li$_{2+x}$Si ↔ Li$_{3.5+x}$Si reaction. It occurs close to the cut-off potential in the cathodic direction and at 0.3 V in the anodic direction. At the same time, the a-Si ↔ a Li$_{2+x}$Si signal weakens and shifts towards lower potentials upon lithiation. This increase in lithiation overpotential might be caused by the high resistance of the SEI or by a partial loss of electric wiring causing an increased current density in other parts of the electrode. The combination of both occurrences might also indicate Li trapping in the silicon particles, preventing complete delithiation, as previously described by Rehnlund et al. [41] In the full-cell however, this phenomenon is absent and only minor shifts in the a-Si ↔ a Li$_2$Si reaction are present. In addition, the FIB-SEM analysis in Fig. 6 showed that the shape of the silicon particles has not changed over 100 cycles. The loss of Li inventory in the SEI is the main reason for the capacity fade. The loss of Li will cause lower degrees of lithiation, which alleviates stresses upon cycling, hence causing less material degradation compared to cycling with Li excess in half-cell configuration.

4. Conclusions

Full-cell setups made of citric acid sol-gel synthesised NCA and commercial battery grade silicon have been analysed based on their performance and the failure mechanism has been described. Cells with pristine electrodes showed a high reversible capacity of 160 mAhg^{-1}(NCA) at an anode operating capacity of 1200 mAhg^{-1}(Si), translating to a specific energy of 477 mWhg^{-1} (active materials). Defining 80% remaining capacity as cell death, the cells cycled for 154 cycles at C/2. Prelithiation of the anode to a value of 300 mAhg^{-1}(Si) increased the cycle life to 245 cycles and the specific energy to 583 mWhg^{-1} (active materials). However, prelithiation cannot ultimately stabilise the system but rather counteracts the degradation mainly governed by the

irreversible consumption of active Li ions in the anode SEI. After 400 cycles in harsh full-cell operation, both electrodes showed reasonable cyclability when reconfigured in half-cells. The NCA cathode was at a high SOC (highly delithiated), but it was possible to relithiate it to a value of 140 mAhg^{-1}. It was also possible to lithiate the silicon anode to high levels again, but the rate capability was highly reduced, caused by the thick SEI layer.

Full-cell cycling in three-electrode cells showed that the evolution of the individual electrode potentials is dynamic during cycling at fixed cell cut-off potential, as more and more lithium is consumed. The rising upper potential of the NCA cathode, caused by the sloping profile of silicon, leads to liberation of more Li in each cycle. These liberated Li ions can partly counteract the Li ions lost in the SEI, keeping the CE at high levels. The cycling performance of the cell can be maintained, but at the expense of the integrity of the cathode. Prelithiation of the anode will increase the cyclability of the cell by the addition of more active Li to the system. By cycle resolved dQ/dV analysis we showed that changes in the voltage profile caused by electrode degradation are absent in the full-cell battery when only 1/3 of the theoretical capacity of silicon is exploited. This is caused by alleviation of stresses in the electrode, as fewer Li ions are available with cycling. Electrode degradation by particle pulverisation or cracking, which is often reported in half-cells is not visible in a full-cell. However, the silicon voltage profile in half-cell configuration after 400 full-cell cycles suggests that this challenge must be handled if it is possible to stabilise the SEI and hence hinder Li loss.

Appendix A. Supplementary data

Supplementary data to this article can be found online at https://doi. org/10.1016/j.jpowsour.2019.226884.

References

[1] J.M. Tarascon, M. Armand, Nature 414 (2001) 359–367.
[2] N. Nitta, F. Wu, J.T. Lee, G. Yushin, Mater. Today 18 (2015) 252–264.
[3] V. Etacheri, R. Marom, R. Elazari, G. Salitra, D. Aurbach, Energy Environ. Sci. 4 (2011) 3243–3262.
[4] J.W. Choi, D. Aurbach, Nat. Rev. Mater. 1 (2016) 16013.
[5] K. Cao, T. Jin, L. Yang, L. Jiao, Mater. Chem. Front. 1 (2017) 2213–2242.
[6] M. Wetjen, S. Solchenbach, D. Pritzl, J. Hou, V. Tileli, H.A. Gasteiger, J. Electrochem. Soc. 165 (2018) A1503–A1514.
[7] J. Li, R.B. Lewis, J.R. Dahn, Electrochem. Solid State Lett. 10 (2007) A17–A20.
[8] I. Kovalenko, B. Zdyrko, a. Magasinski, B. Hertzberg, Z. Milicev, R. Burtovyy, I. Luzinov, G. Yushin, Science (80-.). 334 (2011) 75–79.
[9] C. Erk, T. Brezesinski, H. Sommer, R. Schneider, J. Janek, ACS Appl. Mater. Interfaces 5 (2013) 7299–7307.
[10] S. Zeng, D. Liu, Y. Chen, J. Qian, Y. Cao, H. Yang, X. Ai, J. Mater. Chem. A 3 (2015) 9938–9944.
[11] N. Liu, Z. Lu, J. Zhao, M.T. Mcdowell, H.W. Lee, W. Zhao, Y. Cui, Nat. Nanotechnol. 9 (2014) 187–192.
[12] H. Wu, G. Chan, J.W. Choi, I. Ryu, Y. Yao, M.T. Mcdowell, S.W. Lee, A. Jackson, Y. Yang, L. Hu, Y. Cui, Nat. Nanotechnol. 7 (2012) 310–315.
[13] N.S. Choi, K.H. Yew, K.Y. Lee, M. Sung, H. Kim, S.S. Kim, J. Power Sources 161 (2006) 1254–1259.
[14] US5626981A, 1997.
[15] A.L. Michan, B.S. Parimalam, M. Leskes, R.N. Kerber, T. Yoon, C.P. Grey, B.L. Lucht, Chem. Mater. 28 (2016) 8149–8159.
[16] E. Markevich, G. Salitra, D. Aurbach, ACS Energy Lett 2 (2017) 1337–1345.
[17] T. Jaumann, J. Balach, U. Langklotz, V. Sauchuk, M. Fritsch, A. Michaelis, V. Teltevskij, D. Mikhailova, S. Oswald, M. Klose, G. Stephani, R. Hauser, J. Eckert, L. Giebeler, Energy Storage Mater 6 (2017) 26–35.
[18] K. Eom, T. Joshi, A. Bordes, I. Do, T.F. Fuller, J. Power Sources 249 (2014) 118–124.
[19] Y. Ma, R. Younesi, R. Pan, C. Liu, J. Zhu, B. Wei and K. Edström, 2016, 1–10.
[20] T. Kasukabe, H. Nishihara, K. Kimura, T. Matsumoto, H. Kobayashi, M. Okai, T. Kyotani, Sci. Rep. 7 (2017) 1–10.
[21] C.-H. Yim, S. Niketic, N. Salem, O. Naboka, Y. Abu-Lebdeh, J. Electrochem. Soc. 164 (2017) A6294–A6302.
[22] R. Petibon, V.L. Chevrier, C.P. Aiken, D.S. Hall, S.R. Hyatt, R. Shunmugasundaram, J.R. Dahn, J. Electrochem. Soc. 163 (2016) A1146–A1156.
[23] N. Dupré, P. Moreau, E. De Vito, L. Quazuguel, M. Boniface, A. Bordes, C. Rudisch, P. Bayle-Guillemaud, D. Guyomard, Chem. Mater. 28 (2016) 2557–2572.
[24] S.D. Beattie, M.J. Loveridge, M.J. Lain, S. Ferrari, B.J. Polzin, R. Bhagat, R. Dashwood, J. Power Sources 302 (2016) 426–430.
[25] R.E. Ruther, K.A. Hays, S.J. An, J. Li, D.L. Wood, J. Nanda, ACS Appl. Mater. Interfaces 10 (2018) 18641–18649.
[26] W.M. Dose, V.A. Maroni, M.J. Piernas-Muñoz, S.E. Trask, I. Bloom, C.S. Johnson, J. Electrochem. Soc. 165 (2018) A2389–A2396.
[27] Y. Jin, S. Li, A. Kushima, X. Zheng, Y. Sun, J. Xie, J. Sun, W. Xue, G. Zhou, J. Wu, F. Shi, R. Zhang, Z. Zhu, K. So, Y. Cui, J. Li, Energy Environ. Sci. 10 (2017) 580–592.
[28] D. Mazouzi, B. Lestriez, L. Roué, D. Guyomard, Electrochem. Solid State Lett. 12 (2009) A215.
[29] D. Reyter, S. Rousselot, D. Mazouzi, M. Gauthier, P. Moreau, B. Lestriez, D. Guyomard, L. Roué, J. Power Sources 239 (2013) 308–314.
[30] S.I. Raider, R. Flitsch, M.J. Palmer, J. Electrochem. Soc. 122 (1975) 413–418.
[31] R. Jung, M. Metzger, D. Haering, S. Solchenbach, C. Marino, N. Tsiouvaras, C. Stinner, H.A. Gasteiger, J. Electrochem. Soc. 163 (2016) A1705–A1716.
[32] B. Key, R. Bhattacharyya, M. Morcrette, V. Seznéc, J.-M. Tarascon, C.P. Grey, V. Sezne, D.P.J. Verne, J. Am. Chem. Soc. 131 (2009) 9239–9249.
[33] C.P. Grey, B. Key, M. Morcrette, J.M. Tarascon, J. Am. Chem. Soc. 133 (2011) 503–512.
[34] K. Ogata, E. Salager, C.J. Kerr, A.E. Fraser, C. Ducati, A.J. Morris, S. Hofmann, C.P. Grey, Nat. Commun. 5 (2014) 1–11.
[35] Q. Huang, M.J. Loveridge, R. Genieser, M.J. Lain, R. Bhagat, Sci. Rep. 8 (2018) 1–9.
[36] X.H. Liu, H. Zheng, L. Zhong, S. Huang, K. Karki, L.Q. Zhang, Y. Liu, A. Kushima, W.T. Liang, J.W. Wang, J.H. Cho, E. Epstein, S. a. Dayeh, S.T. Picraux, T. Zhu, J. Li, J.P. Sullivan, J. Cumings, C. Wang, S.X. Mao, Z.Z. Ye, S. Zhang, J.Y. Huang, Nano Lett. 11 (2011) 3312–3318.
[37] N.P. Wagner, A. Tron, J.R. Tolchard, G. Noia, M. Pawel, J. Power Sources 1 (2019) 486–494.
[38] B. Philippe, R. Dedryveìre, M. Gorgoi, H. Rensmo, D. Gonbeau, K. Edström, J. Am. Chem. Soc. 135 (2013) 9829–9842.
[39] M. Wetjen, M. Trunk, L. Werner, R. Gernhäuser, B. Märkisch, Z. Révay, R. Gilles, H.A. Gasteiger, J. Electrochem. Soc. 165 (2018) A2340–A2348.
[40] K. Kleiner, D. Dixon, P. Jakes, J. Melke, M. Yavuz, C. Roth, K. Nikolowski, V. Liebau, Helmut Ehrenberg, J. Power Sources 273 (2015) 70–82.
[41] D. Rehnlund, F. Lindgren, S. Böhme, T. Nordh, Y. Zou, J. Pettersson, U. Bexell, M. Boman, K. Edström, L. Nyholm, Energy Environ. Sci. 10 (2017) 1350–1357.